Journal of Manufacturing Innovations

DOI: 10.22055/JOMI.2025.51453.1033

Vacuum Arc Remelting of WMoNbTa alloys from Elemental Powders: Feasibility, microstructure, mechanical properties, corrosion and wear behavior

J.Naseri [1], G.H. Borhani [1*], K. Ranjbar [2]

[1] Department of Materials Engineering, Malek Ashtar University of Technology, Isfahan, Iran

[2] Department of Materials Science and Engineering, Faculty of Engineering, Shahid Chamran University of Ahvaz, Ahvaz, Iran

ABSTRACT

The present work examines the fabrication, microstructural characteristics, mechanical performance, and corrosion resistance of two refractory high-entropy alloys: $W_{25}Mo_{25}Nb_{25}Ta_{25}$ and $W_{22.5}Mo_{22.5}Nb_{22.5}Ta_{22.5}V_{10}$. The alloys were successfully fabricated from high-purity elemental powders using a two-stage arc melting procedure to ensure high homogeneity. Thermodynamic analysis confirmed that both alloys exhibit parameters favorable for the formation of a disordered Body-Centered Cubic (BCC) solid solution. The addition of 10 at.% vanadium was found to be a potent microstructural modifier, leading to significant refinement and the formation of V-rich secondary phases. This microstructural evolution resulted in a substantial enhancement of the alloy's mechanical properties; the vanadium-modified HEA showed a 42.2% increase in hardness and a yield strength of 1280 MPa, outperforming the base alloy.Electrochemical analysis revealed the remarkable corrosion resistance of both alloys, particularly the $W_{22.5}Mo_{22.5}Nb_{22.5}Ta_{22.5}V_{10}$ alloy, which demonstrated a 15.7-fold reduction in corrosion rate compared to the base alloy. This exceptional resistance is attributed to vanadium's role in stabilizing protective passive films and homogenizing the matrix. Addition of vanadium to the base alloy improved wear behavior and change wear mechanism from adhesive to abrasive wear. However, the presence of secondary phases creating micro-galvanic couples was identified as a limiting factor in further corrosion properties. The findings highlight the significant potential of these vanadium-modified refractory HEAs made from powder feedstock for use in demanding structural and corrosive environments.

ARTICLE HISTORY
Received 24 December 2025
Revised 28 December 2025
Accepted 1 January 2026

KEYWORDS
Refractory high entropy alloys,
RHEAs,
corrosion behavior,
mechanical properties,
high entropy alloys,
microstructure.

1. Introduction

High-entropy alloys (HEAs) constitute an innovative category of materials within the field of materials science, distinguished by their distinctive compositional design and remarkable properties. Whereas conventional alloys typically contain one or two dominant elements with only small amounts of other components, high-entropy alloys consist of several principal elements—usually five or more—present in roughly equal atomic ratios. This approach yields elevated configurational entropy, which promotes the formation of stable solid solution phases and provides outstanding characteristics, including high strength, good ductility, resistance to corrosion, and thermal robustness [1, 2]. In 2004, Jien-Wei Yeh introduced the idea of HEAs, which has since attracted considerable research interest due to their promising uses in fields such as aerospace, automotive, energy, and biomedical industries.[3–5]. A specialized subset of HEAs, known as refractory high-entropy alloys (RHEAs), is designed for high-temperature applications. RHEAs are composed primarily of refractory elements with high melting points, such as tungsten (W), molybdenum (Mo), tantalum (Ta), and niobium (Nb). These alloys exhibit superior mechanical properties and thermal stability, making them promising candidates to replace nickel-based superalloys in extreme environments, such as aerospace and nuclear reactors, where operating temperatures often exceed 1300°C [6–8]. However, RHEAs often possess a body-centered cubic (BCC) structure, which can lead to brittleness, necessitating strategies to balance high strength with adequate ductility [9]. The

* Corresponding author.
E-mail address: borhani_g@yahoo.co.uk, borhanigholam@gmail.com (G.H. Borhani)

WMoTaNb alloy, a refractory HEA, is of particular interest due to its potential for high-temperature structural applications. Comprising tungsten, molybdenum, tantalum, and niobium, this alloy has been studied for its high yield strength and thermal stability. Research has demonstrated that WMoTaNb can be fabricated using various methods, including powder metallurgy techniques such as self-propagating high-temperature synthesis (SHS) [10] and spark plasma sintering (SPS), which allow for precise control over microstructure and composition [11]. Additionally, vacuum arc melting (VAM) using elemental powders as feedstock has been explored for producing WMoTaNb and similar HEAs, offering high purity and rapid solidification to form solid solution phases[12]. While vacuum arc remelting (VAR) typically involves solid electrodes, VAM with powders may be feasible approach for fabricating WMoTaNb, aligning with the need for high-purity, homogeneous alloys, as it was done through powder metallurgy and mechanical alloying approach [13] .Fabrication methods for HEAs and RHEAs are diverse, each with distinct advantages. Vacuum arc melting (VAM) involves melting elemental powders or ingots in a vacuum using an electric arc, ensuring minimal contamination and promoting uniform microstructures [14]. Powder metallurgy, including SHS and SPS, enables the production of dense alloys from oxide precursors, as demonstrated in WMoTaNb fabrication [13]. Other methods, such as laser cladding and additive manufacturing, have been used to produce RHEA coatings and bulk materials [15, 16]. Related alloys, such as NbMoTaW and TiMoTaNbV, provide insights into compositional and processing effects on microstructure and properties [17]. The remarkable mechanical properties of refractory high-entropy alloys (RHEAs) at elevated temperatures have attracted considerable attention in the field of materials science. A primary strategy for enhancing these properties is the modification of alloy composition. In particular, the incorporation of elements such as Ti [18], Zr [19], and Hf [20] has resulted in significant improvements.

The incorporation of solute atoms, notably vanadium, induces substantial lattice dilatation in refractory high-entropy alloys (RHEAs), thereby markedly elevating the strength of both body-centered cubic (BCC) and face-centered cubic (FCC) systems [21].

Studies show that the vanadium content plays a key role in determining microstructural development and the resulting mechanical behavior. As an example, in $NbTiV_xZr$ alloys, lower vanadium contents favor a single-phase BCC solid solution. In contrast, higher levels (e.g., $x \geq 0.75$) cause the breakdown of this phase, resulting in the formation of grain-boundary precipitates rich in V and Zr [22].

Additional studies on Ti_3ZrNbV_x RHEAs show that gradually raising the vanadium content improves the stability of the BCC phase, optimizes mechanical characteristics, and causes a slight rise in density, while at the same time lowering the lattice constants [23]. Vanadium also affects corrosion behavior, as demonstrated in AlCoCrFeNi-derived alloy systems. The vanadium-containing variant (AlCoCrFeNiV) displays superior resistance to corrosion, which is attributed to its refined microstructure and the development of a stable protective surface layer [24] .

The present work examines the production of WMoTaNb refractory high-entropy alloys via vacuum arc remelting of powder-based feedstocks, assessing the process viability, the resultant microstructural features, as well as the mechanical and corrosion performance.

2. Materials and Methods

The synthesis of the Mo-Ta-Nb-W-V alloys commenced with the preparation of high-purity metallic powders, specifically Molybdenum, Tantalum, Niobium, and Tungsten, Vanadium each boasting a purity exceeding 99.8% and an average particle size ranging from 30-40 micrometers. These elemental powders were precisely weighed according to their respective stoichiometric ratios and then individually compacted into discs under pressures between 500-600 MPa. This initial compaction step was crucial for preparing the raw materials for subsequent melting processes.

Following compaction, the elemental discs underwent a two-stage arc melting procedure. Initially, each compressed powder disc was arc-melted on a water-cooled copper hearth in an argon

atmosphere. Subsequently, all pre-melted elemental materials were combined within a water-cooled crucible and subjected to vacuum arc melting. To achieve a high degree of elemental homogeneity throughout the alloy, the resulting ingots were systematically flipped and remelted five times. This meticulous process yielded an alloy ingot approximately 6 mm thick and 25 mm in diameter.

X-ray diffraction (XRD) using Cu-Kα radiation was employed to identify the phase constituents of the arc-melted alloys. Patterns were collected over a 2θ range of 20° to 90°, with a step increment of 0.02° and a scanning speed of 4° per minute.

For microstructural examination, specimens underwent careful surface preparation. This consisted of successive grinding using progressively finer silicon carbide abrasive papers, ending at 3000 grit, followed by polishing with alumina powder to obtain a scratch-free, mirror-like finish. After polishing, the specimens were subjected to chemical etching using a mixture of hydrofluoric acid, nitric acid, and deionized water in a volume ratio of 1:1:2 ($HF:HNO_3:H_2O$) to delineate grain boundaries and other microstructural details. The microstructure was then comprehensively characterized using FESEM (TESCAN, Czech Republic). The Vickers hardness of the alloy was assessed on its polished cross-sectional surfaces. Each indentation was performed at room temperature under a 1 kg load maintained for 15 seconds. The reported hardness values are the average of three measurements taken at distinct locations on the sample.. Electrochemical testing of the alloys was performed at room temperature in an aqueous solution of 3.5 wt.% sodium chloride (NaCl), following the ASTM G-5 standard [25]. A conventional three-electrode cell configuration was employed, using an potentiostat/galvanostat device (Auto Lab AUT 84091) for all measurements. The counter, reference, and working electrodes consisted of a platinum rod, an Ag/AgCl electrode, and the alloy specimen (with an exposed surface area of approximately 1 cm^2), respectively. Prior to each test, it let 1800 seconds to allow stabilization of the open-circuit potential (OCP). Once the OCP stabilized, potentiodynamic polarization curves were recorded to evaluate the corrosion reaction kinetics. The potential was scanned from –300 mV to +1000 mV compare to the OCP and rate of 1 mV/s.

A pin-on-disk tribometer meeting the requirements of ASTM G99 was used [26]. The wear rate of each sample was quantified by the amount of mass or volume removed. This value is affected by the normal force, sliding distance, ambient conditions, test methodology, and velocity. For this investigation, a rotating disk made of AISI 52100 steel (65 HRC hardness) served as the abrasive counterpart. Pins were machined from the studied high-entropy alloys. Following a 500-m sliding distance, the pin's mass reduction was calculated. Before initial weighing and after testing, the samples were cleaned with non-chlorinated, residue-free solvents and dried to eliminate any surface impurities. A four-decimal-place analytical balance was used for mass measurements. Finally, the worn surfaces were examined via FESEM to identify the dominant wear mechanisms.

3. Results and Discussion

3.1 Thermodynamic evaluations

Table 1 shows Thermodynamical and physical parameters of $W_{25}Mo_{25}Nb_{25}Ta_{25}$ and $W_{22.5}Mo_{22.5}Nb_{22.5}Ta_{22.5}V_{10}$ alloys. Both the $W_{25}Mo_{25}Nb_{25}Ta_{25}$ and $W_{22.5}Mo_{22.5}Nb_{22.5}Ta_{22.5}V_{10}$ alloys exhibit exceptionally high Ω parameters (11.1 and 13.9, respectively), significantly exceeding the empirical threshold ($\Omega \geq 1.1$) for solid solution formation. This confirms the overwhelming dominance of entropic stabilization ($T_m.\Delta S_{mix}$) over mixing enthalpy in governing phase stability. The composition-weighted mean melting temperature (T_m) decreases from 2884 °C for the base alloy to 2787 °C with 10 at.% vanadium addition, reflecting vanadium's lower melting point. Concurrently, the dimensionless configurational entropy (ΔS_{mix} /R) increases from 1.38 (medium-entropy regime) to 1.57 (high-entropy regime), enhancing the thermodynamic drive toward disordered solid solutions. Critical electronic and structural parameters strongly favor

BCC phase formation. The valence electron concentration (VEC) remains extremely low for both alloys (5.5 for $W_{25}Mo_{25}Nb_{25}Ta_{25}$; 5.4 for $(W_{22.5}Mo_{22.5}Nb_{22.5}Ta_{22.5}V_{10})$, positioning them well below the BCC-stability threshold (VEC < 6.87). This reduction in VEC - attributed to vanadium's lower valence electron count - systematically reinforces BCC stability. The atomic size mismatch stays within moderate levels, showing δ values of 3.2% for the base alloy and 3.5% for the V-containing variant. Both figures lie well under the critical lattice strain limit of $\delta \leq 6.6\%$. The slight rise in δ is attributed to vanadium's smaller atomic radius compared to that of the original refractory elements.

Favorable atomic-scale interactions are evidenced by strongly negative mixing enthalpies (ΔH_{mix}= -3.0 kJ/mol for $W_{25}Mo_{25}Nb_{25}Ta_{25}$; -2.6 kJ/mol for $(W_{22.5}Mo_{22.5}Nb_{22.5}Ta_{22.5}V_{10})$, confirming thermodynamically driven mixing. Collectively, the convergence of these parameters – exceptionally high Ω (entropic dominance), critically low VEC (BCC stabilization), elevated configurational entropy (solid solution favoring), negative ΔH_{mix} (favorable bonding), and controlled δ (manageable lattice strain) – robustly predicts the formation of disordered BCC solid solutions in both alloy systems. The consistency across these established empirical criteria underscores the thermodynamic stability of the BCC phase [27].

Table 1. Thermodynamical and physical parameters of $W_{25}Mo_{25}Nb_{25}Ta_{25}$ and $W_{22.5}Mo_{22.5}Nb_{22.5}Ta_{22.5}V_{10}$ alloys

sample	Ω	δ (%)	$\Delta S_{mix}/R$	VEC	T_m	ΔH_{mix} (kJ/mol)
$W_{25}Mo_{25}Nb_{25}Ta_{25}$	11.1	3.2	1.38	5.5	2884	-3
$W_{22.5}Mo_{22.5}Nb_{22.5}Ta_{22.5}V_{10}$	13.9	3.5	1.57	5.4	2787	-2.6

3.2 Phase analysis

The experimental lattice constants determined by XRD (3.236 Å for $W_{25}Mo_{25}Nb_{25}Ta_{25}$ and 3.229 Å for $(WMoNbTa)_{90}V_{10}$) demonstrate close agreement with theoretical values calculated using Vegard's law [28] (3.229 Å and 3.209 Å, respectively) (Table 2). This alignment confirms the formation of substitutional solid solutions in both alloys, as Vegard's law assumes ideal linear mixing of atomic radii. The marginal deviations (<0.3%) between experimental and theoretical values fall within typical XRD measurement uncertainty, indicating predominantly ideal solid-solution behavior. Vanadium incorporation produces the predicted lattice contraction in both alloy systems, a trend that follows from vanadium's atomic radius (134 pm) being smaller than that of the base refractory metals (W/Mo: 139 pm, Nb/Ta: 143 pm) [29, 30].

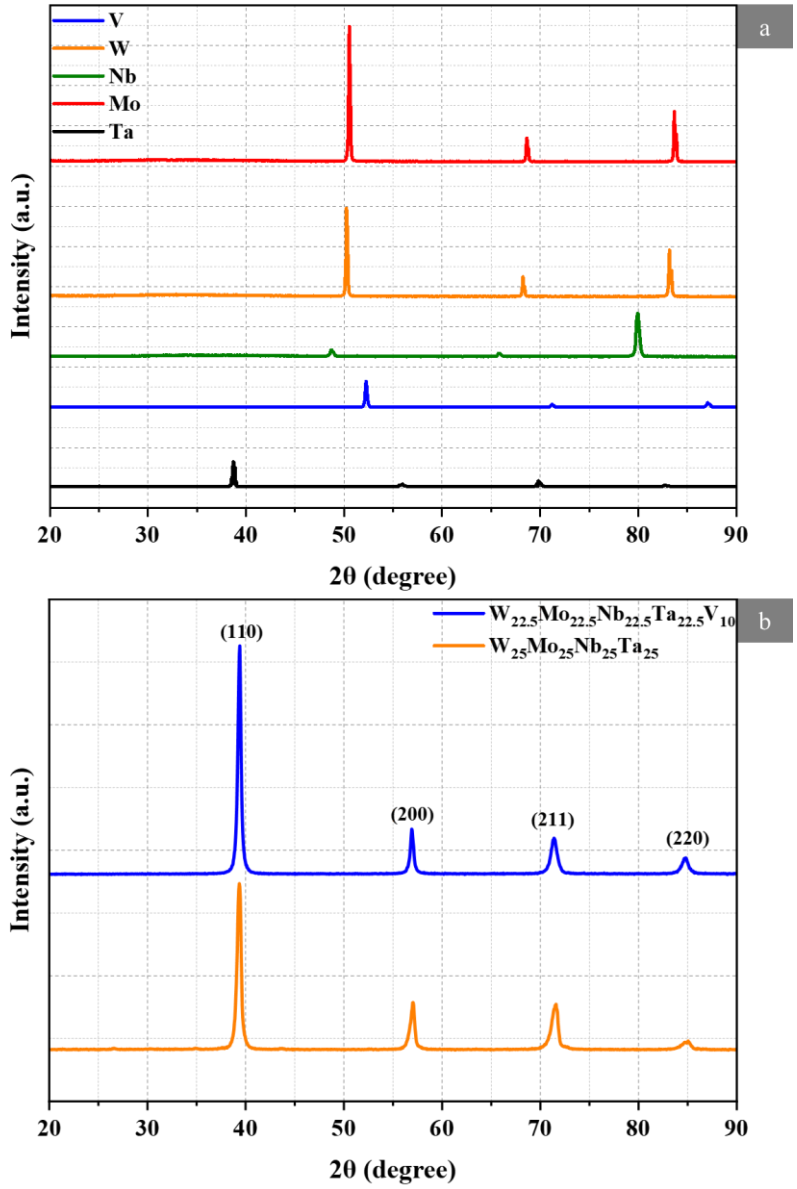


Figure 1. XRD results of a) initial powders used for RHEA fabrication, b) $W_{25}Mo_{25}Nb_{25}Ta_{25}$ and $W_{22.5}Mo_{22.5}Nb_{22.5}Ta_{22.5}V_{10}$ alloys

While the close correspondence generally validates Vegard's law predictions, the systematic positive deviation (experimental > theoretical) in both alloys suggests subtle non-ideal mixing effects. For $W_{25}Mo_{25}Nb_{25}Ta_{25}$, the +0.007 Å difference may arise from residual lattice strains or minor chemical ordering. The larger deviation (+0.020 Å) in $W_{22.5}Mo_{22.5}Nb_{22.5}Ta_{22.5}V_{10}$ implies enhanced lattice distortion due to vanadium's significant size mismatch (δ = 3.5%), potentially involving local atomic relaxations or vacancy formation. This progressive deviation correlates with the alloy's increased configurational entropy ($\Delta S_{mix}/R$ = 1.57), where heightened atomic disorder may amplify local strain fields beyond Vegard's idealized linear approximation.

The addition of vanadium manifests directly in XRD analysis through a systematic rightward shift of diffraction peaks. This shift to higher 2θ angles corresponds to a reduction in interplanar spacing, quantitatively confirming the lattice contraction observed in the refined constants (3.236 Å → 3.230 Å). The peak displacement aligns with Vegard's law predictions and originates from the compressive strain introduced by substituting larger atoms (average radius ~141 pm) with smaller vanadium atoms (134 pm). This consistent behavior across both lattice parameter refinement and peak position analysis provides

complementary evidence of vanadium's solid-solution strengthening effect within the BCC matrix [31].

Table 2. Theoretical and calculated lattice constant from XRD data

sample	Lattice constant (Å)	
	Experimental	Theoretical
$W_{25}Mo_{25}Nb_{25}Ta_{25}$	3.236	3.229
$W_{22.5}Mo_{22.5}Nb_{22.5}Ta_{22.5}V_{10}$	3.226	3.209

3.3 microstructural evaluations

Figure 2 shows OM microstructure of $W_{25}Mo_{25}Nb_{25}Ta_{25}$ and $W_{22.5}Mo_{22.5}Nb_{22.5}Ta_{22.5}V_{10}$ RHEAs alloys. Figure 3 shows a pronounced grain-size reduction upon vanadium addition. The unmodified alloy ($W_{25}Mo_{25}Nb_{25}Ta_{25}$, Figure 2a and Figure 2b) displays a coarse dendritic pattern, typical of conventionally solidified refractory alloys under steep thermal gradients. By contrast, introducing 10 at.% vanadium (yielding $W_{22.5}Mo_{22.5}Nb_{22.5}Ta_{22.5}V_{10}$, **Error! Reference source not found.**c and **Error! Reference source not found.**d) leads to a substantially finer microstructure. Moreover, secondary phases—visible as precipitates located along grain boundaries or interdendritic regions (white arrows in **Error! Reference source not found.**d)—appear solely in the V-bearing composition. This combined outcome of grain refinement plus secondary-phase formation is directly linked to the presence of vanadium [32].

The refined microstructure observed in $W_{22.5}Mo_{22.5}Nb_{22.5}Ta_{22.5}V_{10}$ originates from vanadium's function as an effective solute modifier during solidification. Because vanadium has a smaller atomic radius (≈134 pm) than the larger matrix elements, it generates substantial lattice mismatch. This mismatch intensifies undercooling at melted-solid fronts, which restricts dendritic expansion and favors heterogeneous nucleation. Additionally, vanadium's relatively low diffusion coefficient in BCC lattices slows mass transport, thereby suppressing grain coarsening [33]. Finally, the partition coefficient of vanadium (k_V ≈0.8) elevates undercooling, offering a stronger thermodynamic driving force for nucleation and resulting in a higher grain density [34].

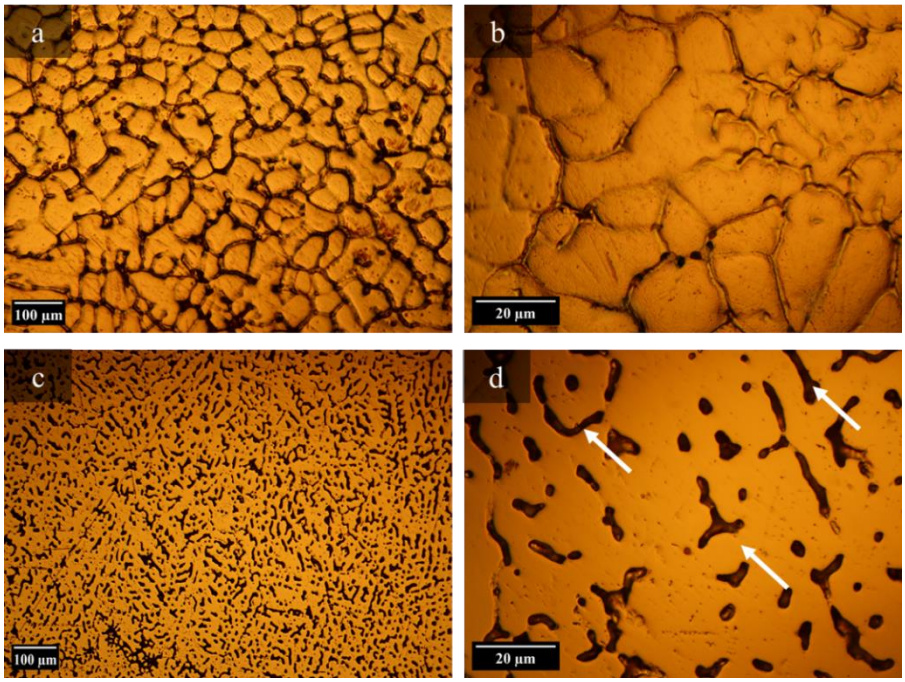


Figure 2. OM microstructure of a,b) $W_{25}Mo_{25}Nb_{25}Ta_{25}$, c,d) and $W_{22.5}Mo_{22.5}Nb_{22.5}Ta_{22.5}V_{10}$

The grain refinement noted in $W_{22.5}Mo_{22.5}Nb_{22.5}Ta_{22.5}V_{10}$ aligns with the reported influence of vanadium in other high-entropy alloy (HEA) systems. Analogous microstructural refinement and reduced elemental segregation have been documented in CoCrFeNi-based and $Al_{0.7}$CoCrFeNi -based HEAs following vanadium addition [35, 36]. In these alloys, vanadium consistently leads to finer, more uniform microstructures and can stabilize certain phases, such as enhancing the stability of the BCC phase. Although secondary phases are present in $W_{22.5}Mo_{22.5}Nb_{22.5}Ta_{22.5}V_{10}$, which were not noted in the referenced systems, this highlights vanadium's complex role as both a grain refiner and a potential precipitate former in refractory HEAs, depending on the specific matrix composition.

Point analysis confirms fundamental differences in phase stability between $W_{25}Mo_{25}Nb_{25}Ta_{25}$ and $W_{22.5}Mo_{22.5}Nb_{22.5}Ta_{22.5}V_{10}$ alloys (Figure 3, Table 3). While WMoNbTa exhibits elemental homogeneity throughout its BCC matrix, the addition of 10 at.% vanadium initiates nucleation of V-rich secondary phases. These discrete precipitates exhibit pronounced compositional partitioning. Energy-dispersive X-ray spectroscopy (EDS) reveals that the precipitates are enriched in vanadium (~33 at.%) and contain high levels of tantalum (~40 at.%) and tungsten (~19 at.%), while the surrounding matrix is dominated by niobium and molybdenum. Such elemental segregation arises from thermodynamic driving forces: the mixing enthalpy between vanadium and tantalum is strongly negative ($\Delta H_{mix}^{V-Ta} \approx$ -1 kJ/mol). In contrast, the positive mixing enthalpy of vanadium with tungsten ($\Delta H_{mix}^{V-W} \approx$ +2 kJ/mol) indicates that tungsten's presence in the precipitates is likely due to kinetic trapping during the solidification process. Vanadium critically accelerates phase evolution through enhanced diffusion kinetics. Its smaller atomic radius facilitates vacancy-mediated diffusion, enabling rapid solute redistribution in $W_{22.5}Mo_{22.5}Nb_{22.5}Ta_{22.5}V_{10}$. This promotes growth of initial Ta-V clusters into discrete precipitates observed at 10 at.% V concentration.

The stability of $W_{22.5}Mo_{22.5}Nb_{22.5}Ta_{22.5}V_{10}$'s secondary phases stems from atomic size compensation mechanisms. While the overall alloy maintains moderate atomic mismatch (δ = 3.5%), localized compositional extremes in precipitates exceed solid solution stability thresholds. The combination of Ta, V, and W accomplishes a crucial size balance. Tantalum's large atomic radius (143 pm) offsets the small radius of vanadium, while tungsten helps accommodate the lattice mismatch at the interface between the precipitates and the rich matrix with Nb and Mo. This collective size adjustment lowers the total system energy more efficiently than the single-phase solid solution present in $W_{25}Mo_{25}Nb_{25}Ta_{25}$. Consequently, vanadium exhibits a dual function—it not only destabilizes the solid-solution structure but also facilitates the formation of more complex phase equilibria.

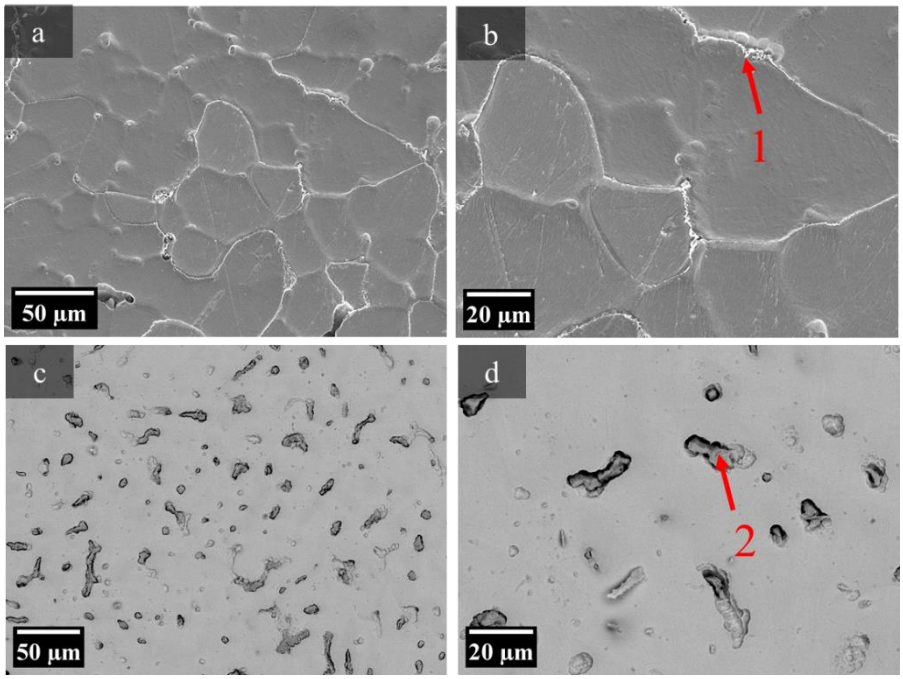


Figure 3. FESEM microstructure of a,b) $W_{25}Mo_{25}Nb_{25}Ta_{25}$, c,d) $W_{22.5}Mo_{22.5}Nb_{22.5}Ta_{22.5}V_{10}$.

Table 3. EDS point analysis of phases shown in Figure 3.

alloys	Points	Chemical composition (at.%)				
		W	Mo	Nb	Ta	V
$W_{25}Mo_{25}Nb_{25}Ta_{25}$	1	19	26.3	29.9	24.8	0
$W_{22.5}Mo_{22.5}Nb_{22.5}Ta_{22.5}V_{10}$	2	19.0	4.1	2.7	40.6	33.7

3.4 Mechanical properties

Figure 4 and table 4 shows the result of compression test and hardness of $W_{25}Mo_{25}Nb_{25}Ta_{25}$ and $W_{22.5}Mo_{22.5}Nb_{22.5}Ta_{22.5}V_{10}$ alloys. The addition of 10 at.% vanadium significantly enhances the ambient temperature mechanical properties of the refractory high-entropy alloy. As shown in Table 4, the yield strength increases from 1170 MPa for the base $W_{25}Mo_{25}Nb_{25}Ta_{25}$ alloy to 1280 MPa for the $W_{22.5}Mo_{22.5}Nb_{22.5}Ta_{22.5}V_{10}$ alloy. A more pronounced improvement is observed in hardness, which rises dramatically from 428 Hv to 609 Hv This represents a 42.2% increase in hardness, demonstrating vanadium's potent strengthening effect.

The marked performance enhancement observed in the $W_{22.5}Mo_{22.5}Nb_{22.5}Ta_{22.5}V_{10}$ alloy arises from the combined effects of solid-solution strengthening and grain refinement. Owing to vanadium's smaller atomic radius compared to the other refractory elements, substantial lattice distortion is induced within the BCC matrix. These distortions generate localized elastic strain fields that effectively hinder dislocation movement. At the same time, microstructural observations reveal a progressive grain-size reduction, shifting from the coarse dendritic morphology of $W_{25}Mo_{25}Nb_{25}Ta_{25}$ to a finer, more equiaxed structure in the vanadium-containing alloy. The resulting increase in grain boundary density serves as an efficient obstacle to the transmission of dislocation slip [12, 37]. These combined mechanisms operate effectively within the single-phase BCC structure maintained at 10 at.% V, maximizing their contribution to strength and hardness without the complication of secondary phases.

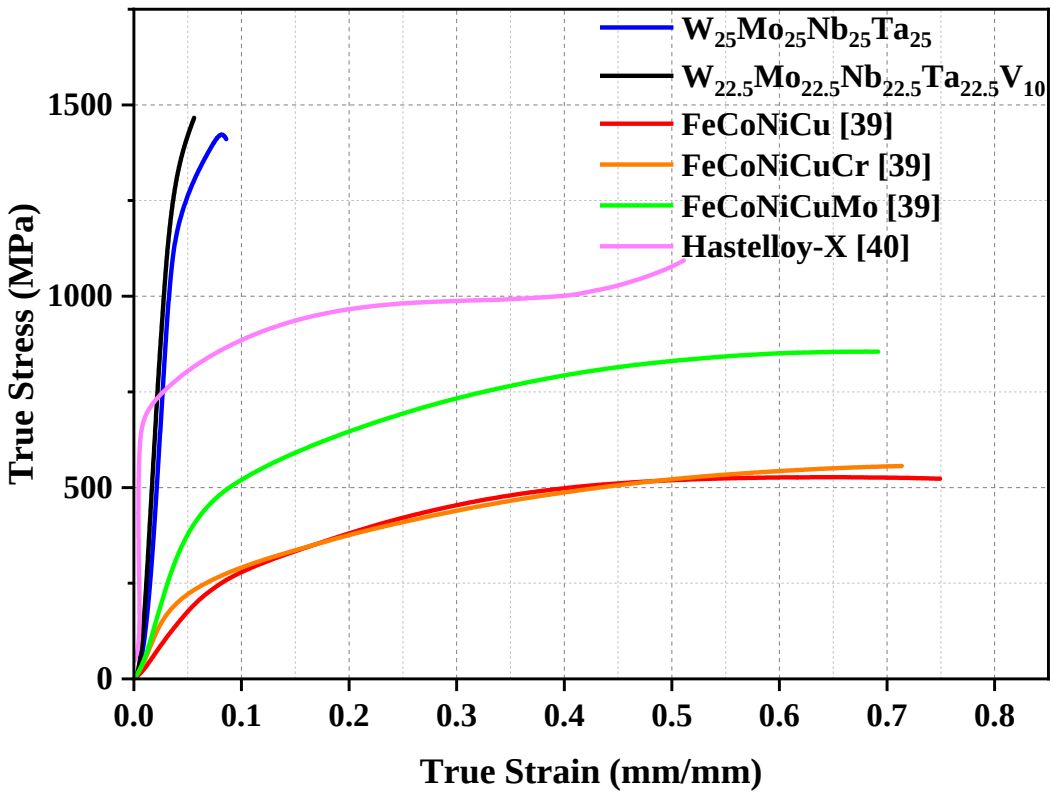


Figure 4. Compressive true stress-strain curves of $W_{25}Mo_{25}Nb_{25}Ta_{25}$, c,d) $W_{22.5}Mo_{22.5}Nb_{22.5}Ta_{22.5}V_{10}$ RHEAs and comparion with other HEAs and convensional alloy.

The mechanical performance of both the $W_{25}Mo_{25}Nb_{25}Ta_{25}$ and $W_{22.5}Mo_{22.5}Nb_{22.5}Ta_{22.5}V_{10}$ alloys far surpasses that of many conventional alloys. As benchmarked in Table 4, the yield strength of the base $W_{25}Mo_{25}Nb_{25}Ta_{25}$ alloy (1170 MPa) is already approximately 6.9 times higher than FeCoNiCu (170 MPa) and 1.7 times higher than Hastelloy-X [38] (673 MPa). The $W_{22.5}Mo_{22.5}Nb_{22.5}Ta_{22.5}V_{10}$ alloy's yield strength (1280 MPa) extends this superiority further. More strikingly, the hardness of the $W_{22.5}Mo_{22.5}Nb_{22.5}Ta_{22.5}V_{10}$ alloy (609 Hv) is 3.4 times higher than FeCoNiCu [39](180 Hv), 2.6 times higher than FeCoNiCuCr (235 Hv), 1.6 times higher than FeCoNiCuMo[39] (381 Hv), and 2.5 times higher than Hastelloy-X (242 Hv). This exceptional combination of yield strength and hardness underscores the potential of these vanadium-modified refractory complex concentrated alloys for demanding structural applications.

Table 4. results of compression test and hardness of $W_{25}Mo_{25}Nb_{25}Ta_{25}$, c,d) $W_{22.5}Mo_{22.5}Nb_{22.5}Ta_{22.5}V_{10}$ RHEAs and comparion with other HEAs and convensional alloy.

sample	Yield stress (MPa)	Hardness (Hv)	Reference
$W_{25}Mo_{25}Nb_{25}Ta_{25}$	1170±8	428±8	Current work
$W_{22.5}Mo_{22.5}Nb_{22.5}Ta_{22.5}V_{10}$	1278± 7	609±12	Current work
FeCoNiCu	170	180	[39]
FeCoNiCuCr	165	235	[39]
FeCoNiCuMo	330	381	[39]
Hastelloy-X	673.3	242	[38, 40]

3.4 Corrosion beahvior

The corrosion behavior of $W_{25}Mo_{25}Nb_{25}Ta_{25}$ and $W_{22.5}Mo_{22.5}Nb_{22.5}Ta_{22.5}V_{10}$ alloys reveals fundamentally different electrochemical responses (Figure 5). The $W_{25}Mo_{25}Nb_{25}Ta_{25}$ alloy exhibits an unusually noble corrosion potential (E_{corr}= 0.26 V) but paradoxically high corrosion current density (i_{corr}= 0.72 µA/cm²), indicating poor passivation stability despite its thermodynamically favorable position. This behavior implies active surface dissolution, likely driven by localized film breakdown, pitting in the base alloy composition. Conversely, the $W_{22.5}Mo_{22.5}Nb_{22.5}Ta_{22.5}V_{10}$ alloy exhibits markedly enhanced corrosion resistance, characterized by a substantially lower current density (i_{corr}= 0.046 µA/cm²) despite its more noble (more negative) corrosion potential (E_{corr}= -0.1 V). This corresponds to a 15.7-fold reduction in corrosion rate relative to $W_{25}Mo_{25}Nb_{25}Ta_{25}$.

The outstanding corrosion resistance of $W_{22.5}Mo_{22.5}Nb_{22.5}Ta_{22.5}V_{10}$ originates from vanadium's two-fold influence on the microstructure [41]. First, vanadium promotes a more uniform alloy matrix, suppressing elemental segregation that otherwise creates easy dissolution paths in the V-free alloy. Second, it enhances the formation and stability of protective passive films rich in Mo and Ta, which effectively hinder chloride ion attack [42].

Both alloys demonstrate exceptional corrosion resistance compared to conventional materials. The $W_{22.5}Mo_{22.5}Nb_{22.5}Ta_{22.5}V_{10}$ alloy's corrosion rate (0.046 µA/cm²) is 233 times lower than FeCoNiCuCr (10.72 µA/cm^2) [39], 280 times lower than FeCoNiCuMo (12.88 µA/cm^2)[39], 41 times lower than Hastelloy-X (1.9 µA/cm^2)[38], and 88 times lower than AISI 316 stainless steel (4.07 µA/cm²)[43]. Even the less corrosion-resistant $W_{25}Mo_{25}Nb_{25}Ta_{25}$ alloy (0.72 µA/cm^2) significantly outperforms these references, being 15-18 times more resistant than the benchmark alloys (table 5). This remarkable corrosion resistance, particularly in the vanadium-modified alloy, highlights their potential for demanding environments where both mechanical integrity and chemical stability are critical.

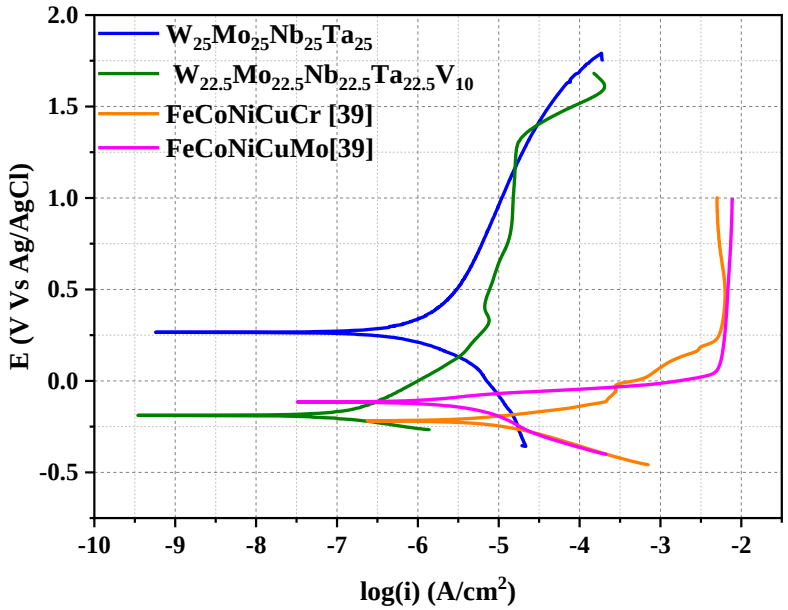


Figure 5. The potentiodynamic polarization curves revealing the electrochemical response of two refractory high-entropy alloys (RHEAs)($W_{25}Mo_{25}Nb_{25}Ta_{25}$ and $W_{22.5}Mo_{22.5}Nb_{22.5}Ta_{22.5}V_{10}$) in a NaCl solution, . These curves also facilitate a comparison with other HEA compositions and a traditional alloy.

Table 5. Corrosion potential and corrosion current density values for studied $W_{25}Mo_{25}Nb_{25}Ta_{25}$, and $W_{22.5}Mo_{22.5}Nb_{22.5}Ta_{22.5}V_{10}$ RHEAs in NaCl solution and comparion with other HEAs and convensional alloy.

sample	E_{corr} (V)	i_{corr} ($\mu A/cm^2$)	Reference
$W_{25}Mo_{25}Nb_{25}Ta_{25}$	0.26	0.72	Current work
$W_{22.5}Mo_{22.5}Nb_{22.5}Ta_{22.5}V_{10}$	-0.1	0.046	Current work
FeCoNiCuCr	-0.19	10.72	[39]
FeCoNiCuMo	-0.32	12.88	[39]
Hastelloy-X	-0.22	1.9	[38, 40]
AISI 316 Stainless steel	-0.17	4.07	[44]

3.5 Wear behavior

The wear performance of the $W_{25}Mo_{25}Nb_{25}Ta_{25}$ alloy is characterized by a high coefficient of friction (COF = 0.68) and the greatest weight loss (0.0636 g), indicative of an inefficient and damaging tribological response (Figure 6). SEM analysis (Figure 7) of its worn surface reveals a morphology dominated by severe adhesive wear. The evidence consists of widespread plastic flow, significant smearing of material across the surface, and large-scale adhesive wear fragments. The coarse, dendritic microstructure and relatively low hardness (428Hv) of the $W_{25}Mo_{25}Nb_{25}Ta_{25}$ alloy facilitate significant subsurface plastic flow under sliding contact. This allows strong adhesive junctions to form with the counterface, which are subsequently sheared off, leading to considerable material transfer and loss. The high friction is a direct result of the energy required to continuously shear these metallic bonds and plow through the softened surface layers.

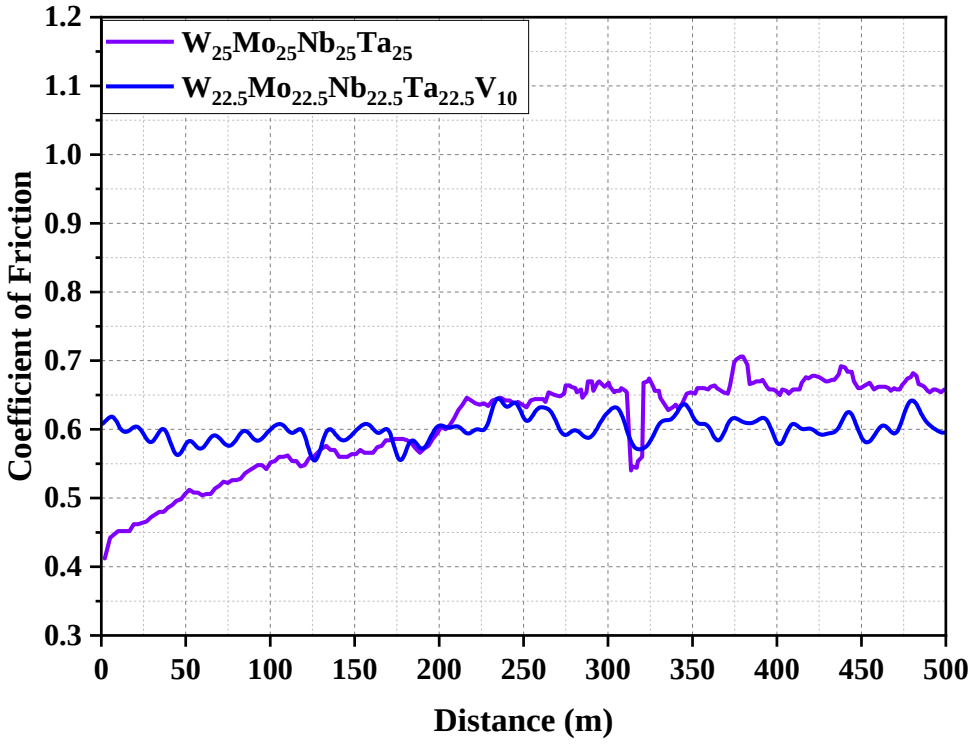


Figure 6. coefficient of friction variations of $W_{25}Mo_{25}Nb_{25}Ta_{25}$, and $W_{22.5}Mo_{22.5}Nb_{22.5}Ta_{22.5}V_{10}$ RHEAs.

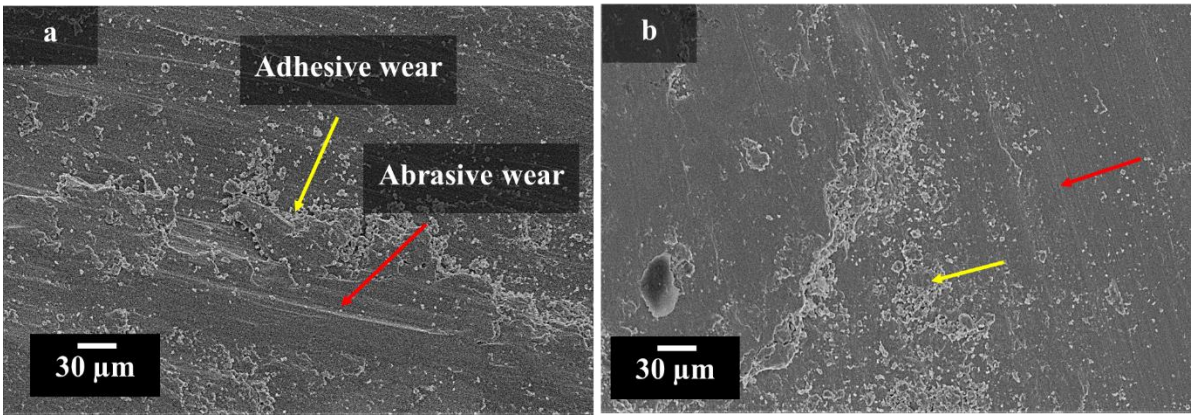


Figure 7. SEM micrographs of worn surface for a) $W_{25}Mo_{25}Nb_{25}Ta_{25}$, b) $W_{22.5}Mo_{22.5}Nb_{22.5}Ta_{22.5}V_{10}$ RHEAs.

In contrast, the $W_{22.5}Mo_{22.5}Nb_{22.5}Ta_{22.5}V_{10}$ alloy demonstrates a marked improvement, with a reduced COF (0.612) and lower weight loss (0.0423 g). The corresponding worn surface morphology shows a transition to a mixed adhesive-abrasive wear mechanism. While some adhesive features persist, the surface is primarily marked by finer, more parallel grooves and a notable reduction in severe plastic deformation and large adhesive craters. This shift is a direct consequence of the vanadium-induced microstructural refinement. The solid-solution strengthening and grain refinement in $W_{22.5}Mo_{22.5}Nb_{22.5}Ta_{22.5}V_{10}$ significantly increase its hardness (609 Hv) and yield strength, making the surface more resistant to adhesive junction formation and subsurface plastic flow. Consequently, material removal occurs through a milder process of micro-plowing and micro-cutting[45].

The direct comparison between $W_{25}Mo_{25}Nb_{25}Ta_{25}$ and $W_{22.5}Mo_{22.5}Nb_{22.5}Ta_{22.5}V_{10}$ highlights the critical impact of vanadium's solid-solution role. The 29% reduction in wear loss and the 9%

decrease in COF from $W_{25}Mo_{25}Nb_{25}Ta_{25}$ to $W_{22.5}Mo_{22.5}Nb_{22.5}Ta_{22.5}V_{10}$ are quantitatively linked to the change in dominant damage mode [46]. The adhesive-dominated wear in $W_{25}Mo_{25}Nb_{25}Ta_{25}$ is inherently unstable and results in high, fluctuating friction coupled with large material transfer. The abrasive-dominated wear in $W_{22.5}Mo_{22.5}Nb_{22.5}Ta_{22.5}V_{10}$, while still causing material loss, is a more stable and controlled process. The harder surface of $W_{22.5}Mo_{22.5}Nb_{22.5}Ta_{22.5}V_{10}$ reduces the real area of contact and the shear strength of any adhesive junctions that do form, leading to a smoother sliding interaction and less energy dissipation as friction and heat.

The underlying mechanism for this improvement is rooted in the microstructural homogeneity achieved at 10 at.% vanadium. At this composition, vanadium is fully dissolved in the BCC matrix, creating a single-phase, chemically homogeneous solid solution [47]. This eliminates weak secondary phases or severe chemical segregation that could act as initiation sites for delamination. The resulting uniform high hardness allows the $W_{22.5}Mo_{22.5}Nb_{22.5}Ta_{22.5}V_{10}$ alloy to resist penetration and deformation from the counterface, forcing the tribological system into a regime of mild abrasion. This analysis confirms that even without forming a composite structure, optimizing the solid-solution state through vanadium addition is a highly effective strategy for transitioning from severe adhesive wear to a more benign and controllable wear mode, thereby enhancing overall tribological performance.

4. Conclusions

In this study, WMoNbTa alloys were synthesized through a meticulous two-stage arc melting procedure using high-purity elemental powders. The researchers then performed a comprehensive characterization of the resulting alloys. X-ray Diffraction (XRD) was used to analyze the phase composition and lattice parameters, and OM and FESEM to evaluate the microstructure. Finally, the mechanical properties were assessed through compression test and hardness measurements, and the corrosion behavior was investigated to understand the impact of vanadium addition on the overall performance of the alloys. Here is the highlighted results:

1- The study successfully demonstrated the synthesis of complex WMoNbTa alloys from high-purity elemental powders using a two-stage arc melting procedure, resulting in a homogeneous ingot.

2- The thermodynamic analysis confirmed that both the base $W_{25}Mo_{25}Nb_{25}Ta_{25}$ alloy and the vanadium-modified $(WMoNbTa)_{90}V_{10}$ alloy possess exceptionally high Ω parameters (≥ 1.1) and low Valence Electron Concentrations (VEC < 6.87), which robustly predicts the formation and stability of a disordered Body-Centered Cubic (BCC) solid solution.

3- The addition of 10 at.% vanadium was found to significantly refine the microstructure, transitioning the alloy from a coarse dendritic morphology to a finer structure. This is attributed to vanadium's role as a potent solute modifier that enhances constitutional undercooling and hinders grain coarsening during solidification.

4- The vanadium-modified alloy, $(WMoNbTa)_{90}V_{10}$, demonstrated a substantial improvement in mechanical properties. Its yield strength increased to 1276.6 MPa and hardness rose dramatically to 608.7 Hv, representing a 42.2% increase compared to the base alloy. This enhancement is a result of synergistic solid solution strengthening and the observed grain refinement.

5- Both $W_{25}Mo_{25}Nb_{25}Ta_{25}$ and the vanadium-modified alloy exhibit remarkable corrosion resistance compared to conventional materials like AISI 316 stainless steel and Hastelloy-X. The $(WMoNbTa)_{90}V_{10}$ alloy's corrosion rate (0.046μA/cm2) is hundreds of times lower than these benchmark materials.

6- The addition of 10 at.% vanadium led to a 15.7-fold decrease in the corrosion rate of the alloy compared to the base $W_{25}Mo_{25}Nb_{25}Ta_{25}$. This highlights vanadium's critical role in significantly improving the alloy's performance in corrosive environments.

7- Addition of Vanadium improved wear resistance and changed wear mechanim from mostly adhesive wear to a mixed adhesive-abrasive wear behavior.

References

[1] Y. Zhang and W. J. Peng, "Microstructural control and properties optimization of high-entrop alloys," *Procedia Eng*, vol. 27, pp. 1169–1178, 2012, doi:10.1016/j.proeng.2011.12.568

[2] J. Chen *et al.*, "A review on fundamental of high entropy alloys with promising high–temperature properties," *J Alloys Compd*, vol. 760, pp. 15–30, 2018, doi:10.1016/J.JALLCOM.2018.05.067

[3] J. W. Yeh *et al.*, "Nanostructured High-Entropy Alloys with Multiple Principal Elements: Novel Alloy Design Concepts and Outcomes," *Adv Eng Mater*, vol. 6, no. 5, pp. 299–303, 2004, doi:10.1002/ADEM.200300567

[4] D. B. Miracle and O. N. Senkov, "A critical review of high entropy alloys and related concepts," *Acta Mater*, vol. 122, pp. 448–511, 2017, doi:10.1016/J.ACTAMAT.2016.08.081

[5] E. P. George, W. A. Curtin, and C. C. Tasan, "High entropy alloys: A focused review of mechanical properties and deformation mechanisms," *Acta Mater*, vol. 188, pp. 435–474, 2020, doi:10.1016/j.actamat.2019.12.015

[6] G. W. D. M. C. C. P. L. ON Senkov, "Refractory high-entropy alloys," *Intermetallics (Barking)*, vol. 18, pp. 1758–1765, 2010.

[7] L. Lilensten, "New structure in refractory high-entropy alloys," *Mater. Lett.*, vol. 132, pp. 123–125, 2014.

[8] O. N. Senkov, S. Gorsse, and D. B. Miracle, "High temperature strength of refractory complex concentrated alloys," *Acta Mater*, vol. 175, pp. 394–405, 2019, doi:10.1016/j.actamat.2019.06.032

[9] F. Liu, P. K. Liaw, and Y. Zhang, "Recent Progress with BCC-Structured High-Entropy Alloys," *Metals (Basel)*, vol. 12, no. 3, 2022, doi:10.3390/MET12030501

[10] E. Nikolay, M. Alexey, B. Ivan, and Z. Ilya, "Self-propagating high-temperature synthesis of high-entropy ceramic composition (Hf0.25Ti0.25Cr0.25(FeV)0.25)N," *Mater Lett*, vol. 346, p. 134562, 2023, doi:10.1016/J.MATLET.2023.134562

[11] Q. Liu, G. Wang, X. Sui, Y. Liu, X. Li, and J. Yang, "Microstructure and mechanical properties of ultra-fine grained MoNbTaTiV refractory high-entropy alloy fabricated by spark plasma sintering," *J Mater Sci Technol*, vol. 35, no. 11, pp. 2600–2607, 2019, doi:10.1016/j.jmst.2019.07.013

[12] L. Raman *et al.*, "Strengthening mechanisms in CrMoNbTiW refractory high entropy alloy," *Materials Science and Engineering: A*, vol. 819, 2021, doi:10.1016/j.msea.2021.141503

[13] M. Moser *et al.*, "Elaboration and Characterization of WMoTaNb High Entropy Alloy Prepared by Powder Metallurgy Processes," *Materials 2022, Vol. 15, Page 5416*, vol. 15, no. 15, p. 5416, 2022, doi:10.3390/MA15155416

[14] J. Zhang *et al.*, "Microstructure and mechanical properties of RexNbMoTaW high-entropy alloys prepared by arc melting using metal powders," *J Alloys Compd*, vol. 827, 2020, doi:10.1016/j.jallcom.2020.154301

[15] X. Liu, L. Zhong, Y. Chen, L. Chai, S. Guo, and N. Guo, "Corrosion and oxidation behaviors of CoAlTiWTa RHEA coating on Inconel 718

superalloy prepared by laser cladding," *Corros Sci*, vol. 236, p. 112273, 2024, doi:10.1016/J.CORSCI.2024.112273

[16] Y. Li, L. Chen, L. Lu, X. Zhang, W. Zhou, and X. Ren, "Numerical and experimental study of RHEAs surface morphology and defect in selective laser melting," *Int J Refract Metals Hard Mater*, vol. 118, p. 106484, 2024, doi:10.1016/J.IJRMHM.2023.106484

[17] X. G. Li, C. Chen, H. Zheng, Y. Zuo, and S. P. Ong, "Complex strengthening mechanisms in the NbMoTaW multi-principal element alloy," *NPJ Comput Mater*, vol. 6, no. 1, pp. 1–10, 2020, doi:10.1038/S41524-020-0339-0

[18] Z. D. Han *et al.*, "Effect of Ti additions on mechanical properties of NbMoTaW and VNbMoTaW refractory high entropy alloys," *Intermetallics (Barking)*, vol. 84, pp. 153–157, 2017, doi:10.1016/j.intermet.2017.01.007

[19] T. Li *et al.*, "A novel ZrNbMoTaW refractory high-entropy alloy with in-situ forming heterogeneous structure," *Materials Science and Engineering: A*, vol. 827, 2021, doi:10.1016/J.MSEA.2021.142061

[20] Y. Wan *et al.*, "Superior high-temperature strength in a dual-BCC-phase NbMoTaWHf refractory high-entropy alloy," *Intermetallics (Barking)*, vol. 175, p. 108515, 2024, doi:10.1016/J.INTERMET.2024.108515

[21] F. Alijani, M. Reihanian, and K. Gheisari, "Study on phase formation in magnetic FeCoNiMnV high entropy alloy produced by mechanical alloying," *J Alloys Compd*, vol. 773, pp. 623–630, 2019, doi:10.1016/J.JALLCOM.2018.09.204

[22] X. G. Wang *et al.*, "Effects of vanadium content on the microstructure and tensile properties of NbTiVxZr high-entropy alloys," *J Alloys Compd*, vol. 987, p. 174227, 2024, doi:10.1016/J.JALLCOM.2024.174227

[23] N. Al-Zoubi, A. Almahmoud, and A. Obeidat, "Impact of Vanadium and Zirconium Contents on Properties of Novel Lightweight Ti3ZryNbVx Refractory High-Entropy Alloys," *Solids 2025, Vol. 6, Page 2*, vol. 6, no. 1, p. 2, 2025, doi:10.3390/SOLIDS6010002

[24] C. A. Souto, A. L. R. Mirhan, J. Y. Yao, L. B. Serrano, D. N. Travessa, and K. R. Cardoso, "Microstructural characteristics and corrosion behaviour of AlCoCrFeNi high-entropy alloys containing Vanadium," *Electrochim Acta*, vol. 503, p. 144867, 2024, doi:10.1016/J.ELECTACTA.2024.144867

[25] Astm, "ASTM G5 Standard Reference Test Method for Making Potentiodynamic Anodic Polarization Measurements," *Annual Book of ASTM Standards*, 2014.

[26] ASTM International, "ASTM G99-17, Standard Test Method for Wear Testing with a Pin-on-Disk Apparatus," *Annual Book of ASTM Standards*, 2017.

[27] F. Z. S. C. W. C. C Zhang, "Computational thermodynamics aided high-entropy alloy design," *JOM*, vol. 64, pp. 839–845, 2012.

[28] K. T. Jacob, S. Raj, and L. Rannesh, "Vegard's law: A fundamental relation or an approximation?," *Zeitschrift fuer Metallkunde/Materials Research and Advanced Techniques*, vol. 98, no. 9, pp. 776–779, 2007, doi:10.3139/146.101545/MACHINEREADABLECITATION/RIS

[29] F. G. Coury, M. Kaufman, and A. J. Clarke, "Solid-solution strengthening in refractory high entropy alloys," *Acta Mater*, vol. 175, pp. 66–81, 2019, doi:10.1016/j.actamat.2019.06.006

[30] Y. Zhang, Y. J. Zhou, J. P. Lin, G. L. Chen, and P. K. Liaw, "Solid-solution phase formation rules for multi-component alloys," *Adv Eng Mater*, vol. 10, no. 6, pp. 534–538, 2008, doi:10.1002/adem.200700240

[31] M. Wang, Z. L. Ma, Z. Q. Xu, and X. W. Cheng, "Effects of vanadium concentration on mechanical properties of VxNbMoTa refractory high-entropy alloys," *Materials Science and Engineering: A*, vol. 808, 2021, doi:10.1016/J.MSEA.2021.140848

[32] J. Zhang *et al.*, "Microstructure and mechanical properties of RexNbMoTaW high-entropy alloys prepared by arc melting using metal powders," *J Alloys Compd*, vol. 827, p. 154301, 2020, doi:10.1016/j.jallcom.2020.154301

[33] G. Lindwall and K. Frisk, "Assessment and evaluation of mobilities for diffusion in the bcc Cr-Mo-Fe system," *J Phase Equilibria Diffus*, vol. 33, no. 5, pp. 375–389, 2012, doi:10.1007/S11669-012-0107-Z/FIGURES/20

[34] M. R. Zamani, H. Mirzadeh, M. Malekan, I. Weißensteiner, and M. Roostaei, "Unveiling the strengthening mechanisms of as-cast micro-alloyed CrMnFeCoNi high-entropy alloys," *J Alloys Compd*, vol. 957, p. 170443, 2023, doi:10.1016/J.JALLCOM.2023.170443

[35] Z. G. Zhu, K. H. Ma, Q. Wang, and C. H. Shek, "Compositional dependence of phase formation and mechanical properties in three CoCrFeNi-(Mn/Al/Cu) high entropy alloys," *Intermetallics (Barking)*, vol. 79, pp. 1–11, 2016, doi:10.1016/j.intermet.2016.09.003

[36] X. Zhong, Q. Zhang, F. Jiang, Y. Yan, Z. Wang, and M. Wu, "Microstructural features and excellent compression properties of a novel Al0.7CoCrFeNiTi0.3 high entropy alloy," *Mater Lett*, vol. 286, 2021, doi:10.1016/J.MATLET.2020.129246

[37] L. Zong *et al.*, "Mechanical properties and strengthening mechanism of the nano-sized m-ZrO2 ceramic particle reinforced NbMoTaW refractory high-entropy alloy," *Int J Refract Metals Hard Mater*, vol. 113, 2023, doi:10.1016/j.ijrmhm.2023.106201

[38] K. Ranjbar, M. A. Harb, M. Yeganeh, M. Reihanian, and J. Naseri, "Selective laser melting of Hastelloy-X alloy and cerium oxide reinforced Hastelloy-X composite: Microstructural examination and corrosion behavior," *Journal of Materials Research and Technology*, vol. 30, pp. 7803–7815, 2024, doi:10.1016/J.JMRT.2024.05.126

[39] M. Shirali, Kh. Gheisari, and M. Reihanian, "Phase evolution, mechanical properties, and corrosion behavior of FeCoNiCu-based high-entropy alloys," *Journal of Materials Research and Technology*, vol. 37, pp. 4275–4290, 2025, doi:10.1016/J.JMRT.2025.07.099

[40] K. Ranjbar, M. Reihanian, M. A. Harb, M. Yeganeh, J. Naseri, and Z. Xiaolin, "Microstructure and Texture Evolution of Hastelloy X and CeO2-Hastelloy X Composite Fabricated by Selective Laser Melting," *Metals and Materials International*, pp. 1–14, 2025, doi:10.1007/S12540-025-01910-1/METRICS

[41] Y. Shi, B. Yang, and P. K. Liaw, "Corrosion-resistant high-entropy alloys: A review," *Metals (Basel)*, vol. 7, no. 2, 2017, doi:10.3390/MET7020043

[42] N. Hua *et al.*, "Mechanical, corrosion, and wear properties of biomedical Ti–Zr–Nb–Ta–Mo high entropy alloys," *J Alloys Compd*, vol. 861, 2021, doi:10.1016/J.JALLCOM.2020.157997

[43] F. Andreatta, A. Lanzutti, E. Vaglio, G. Totis, M. Sortino, and L. Fedrizzi, "Corrosion behaviour of 316L stainless steel manufactured by selective laser melting," *Materials and Corrosion*, vol. 70, no. 9, pp. 1633–1645, 2019, doi:10.1002/MACO.201910792

[44] P. A.-M. in tehnologije and undefined 2014, "Comparison of the corrosion behaviour of austenitic stainless steel in seawater and in a 3.5% NaCl solution," *mit.imt.siPKL AVSTENITNIHMateriali in tehnologije, 2014•mit.imt.si* Accessed: Aug. 10, 2025. [Online]. Available: http://mit.imt.si/izvodi/mit146/donik.pdf

[45] Z. Chong *et al.*, "Enhanced wear and corrosion resistances of AlCoCrFeNi high-entropy alloy coatings via high-speed laser cladding," *Mater Today Commun*, vol. 33, 2022, doi:10.1016/j.mtcomm.2022.104417

[46] A. Poulia, C. Mathiou, E. Georgatis, and A. E. Karantzalis, "Microstructural Verification, Mechanical and Wear Analysis of MoTaNbVxTi Refractory High-Entropy Alloys," *Strength of Materials*, vol. 53, no. 6, pp. 1011–1022, 2021, doi:10.1007/S11223-022-00368-5

[47] S. A. Firstov, V. F. Gorban', N. A. Krapivka, M. V. Karpets, and A. D. Kostenko, "Wear Resistance of High-Entropy Alloys," *Powder Metallurgy and Metal Ceramics*, vol. 56, no. 3–4, pp. 158–164, 2017, doi:10.1007/S11106-017-9882-8/METRICS